

2D Mechanical Metamaterials with Widely Tunable Unusual Modes of Thermal Expansion

Xiaoyue Ni, Xiaogang Guo, Jiahong Li, Yonggang Huang, Yihui Zhang,*
and John A. Rogers*

Most natural materials expand uniformly in all directions upon heating. Artificial, engineered systems offer opportunities to tune thermal expansion properties in interesting ways. Previous reports exploit diverse design principles and fabrication techniques to achieve a negative or ultralow coefficient of thermal expansion, but very few demonstrate tunability over different behaviors. This work presents a collection of 2D material structures that exploit bimaterial serpentine lattices with micrometer feature sizes as the basis of a mechanical metamaterials system capable of supporting positive/negative, isotropic/anisotropic, and homogeneous/heterogeneous thermal expansion properties, with additional features in unusual shearing, bending, and gradient modes of thermal expansion. Control over the thermal expansion tensor achieved in this way provides a continuum-mechanics platform for advanced strain-field engineering, including examples of 2D metamaterials that transform into 3D surfaces upon heating. Integrated electrical and optical sources of thermal actuation provide capabilities for reversible shape reconfiguration with response times of less than 1 s, as the basis of dynamically responsive metamaterials.

Upon heating, the interatomic bonds of most solid materials elongate, manifesting as an expansion in volume. Materials that change in shape as a result of heating support a rich range of uses in electronics and optical systems,^[1–4] deployable or morphing structures,^[5–10] and active metamaterials.^[11] These applications motivate interest in systems that offer unconventional thermal expansion behaviors. At the atomic level, thermally activated geometric rotation of molecular units can result in unusual volume changes in bulk solids.^[12–14] Examples are in diyn-diol molecules with tilted space-filling dumbbell shapes and methanol monohydrate with apically linked rhombic lattice geometries, to yield large anisotropic and negative thermal expansion behaviors.^[15,16] By analogy, mechanical or structural interactions between architected constituents

Dr. X. Ni, Prof. Y. Huang, Prof. J. A. Rogers
Center for Bio-Integrated Electronics
Northwestern University
Evanston, IL 60208, USA
E-mail: jrogers@northwestern.edu

Dr. X. Guo, Prof. Y. Zhang
AML
Department of Engineering Mechanics
Center for Flexible Electronics Technology
Tsinghua University
Beijing 100084, China
E-mail: yihuizhang@tsinghua.edu.cn

J. Li, Prof. Y. Huang, Prof. J. A. Rogers
Department of Materials Science and Engineering
Northwestern University
Evanston, IL 60208, USA

Prof. Y. Huang, Prof. J. A. Rogers
Department of Mechanical Engineering
Northwestern University
Evanston, IL 60208, USA

Prof. Y. Huang
Department of Civil and Environmental Engineering
Northwestern University
Evanston, IL 60208, USA

Prof. J. A. Rogers
Simpson Querrey Institute
Northwestern University
Chicago, IL 60611, USA

Prof. J. A. Rogers
Department of Biomedical Engineering
Northwestern University
Evanston, IL 60208, USA

Prof. J. A. Rogers
Department of Chemistry
Northwestern University
Evanston, IL 60208, USA

Prof. J. A. Rogers
Department of Electrical and Computer Engineering
Northwestern University
Evanston, IL 60208, USA

Prof. J. A. Rogers
Department of Neurological Surgery
Northwestern University
Evanston, IL 60208, USA

 The ORCID identification number(s) for the author(s) of this article can be found under <https://doi.org/10.1002/adma.201905405>.

DOI: 10.1002/adma.201905405

with different thermal responses can induce local bending or rotational motions within the available internal free space to yield tunable thermal expansion or contraction responses.^[17–20] The use of engineered 2D and 3D bimaterial lattices or microstructures based on reentrant geometries can produce large isotropic negative coefficients of thermal expansion (CTE), with few, if any, equivalents in naturally occurring materials.^[21–23] These constructs are especially useful in applications that benefit from the ability to balance environmentally induced thermal stresses. Other applications require ultralow CTE for thermal stability, motivating the design of stretch-dominated bimaterial lattices as an effective compensation of volume change.^[24–27]

In 2D, a CTE tensor, α_{ij} , characterizes arbitrary thermal expansion properties as, $\varepsilon_{ij} = \alpha_{ij} \Delta T$, where ε_{ij} is the thermal strain tensor. Previous studies focus only on tuning of the principal-axis coefficients, α_{ii} . In most cases, distinctive geometric rules guide individual designs for positive, negative, and zero values of α_{ij} . None of these platforms grant access to the off-diagonal terms in the CTE tensor, that is, shear modes of thermal expansion. Furthermore, designs for independent tuning on each coefficient for precise control of the degrees of anisotropy are rare. The few existing examples accommodate only limited tunability over expansion behaviors.^[28–33] Simple prototyping techniques rely on welding,^[26] pin-joint,^[24,29–31] or gluing^[33] of bimaterial parts, without scalable means for realistic manufacturing or for rendering microscale features. Alternative schemes that bypass some of these limitations exploit reductive sintering,^[21] thin-film deposition,^[27] stereolithography,^[22,23] and 3D printing,^[29] but each has limitations in materials choices. A notable feature is that published architectures usually involve rigid joints between unit cells, thereby passivating the effects of local deformation on neighboring cells and thus preventing explorations of hierarchical designs for additional design options.

Here, we present a first step toward a generalized design and fabrication strategy to metamaterial systems that can support complex, arbitrary thermal deformations. Specifically, this paper introduces a set of 2D architectures for this purpose through modeling, simulations, and experiments. Here, structural designs that combine planar triangle unit cells composed of bilayer serpentine beams serve as platforms for achieving a broad range of isotropic positive/negative thermal expansion behaviors with additional capabilities in precise control of the degrees of anisotropy, featuring a realization of large isotropic negative, anisotropic positive, and unusual shear CTE. A hierarchical design that exploits a spatially heterogeneous arrangement of unit cells allows access to additional bending and gradient modes of thermal expansion.

The fabrication strategy uses precision laser cutting with micrometer-scale resolution to achieve multimaterial thin films with interfaces that lie in the plane of the 2D structures, as a key to leveraging bending mode actuation from bi-morph beams. Slight adaptations of this 2D manufacturing process yield options in spatial control for thermally induced geometrical transformations from 2D to 3D layouts. This approach offers a robust manufacturing sequence for such bimaterial microstructures, with few intrinsic limitations on the constituent materials. The thin, filamentary geometries and microscale features lead to fast local thermal response times, as well

as facile integration of electrical or optical means for actuation in a spatiotemporally controlled manner. The flexible interconnects promote a continuum-based mechanics of the cellular microstructures for future development in perturbative and reconfigurable metamaterials.

In the designs presented here, curved bilayer beams serve as building blocks. The bilayer structure amplifies the thermal response by translating the differential linear thermal expansion into a bending deflection. Consider an elastic bilayer thin beam (**Figure 1a**, left) with an initial angle θ_0 , radius of curvature R_0 , and composed of different materials on the convex (1; thickness t_1 ; Young's modulus E_1 ; and CTE α_1) and concave (2; thickness t_2 ; Young's modulus E_2 ; and CTE α_2) sides, where the material with larger CTE covers a ratio r ($0 \leq r \leq 1$) of the frame layer. The analytical solution for the effective linear strain ε_T due to a temperature change ΔT is (see Note S1, Supporting Information, for details)

$$\varepsilon_T = \alpha_{\text{meta}} \Delta T = \beta \left(E_1, E_2, \frac{t_1}{R_0}, \frac{t_2}{R_0} \right) f(\theta_0, r) (\alpha_2 - \alpha_1) \Delta T \quad (1)$$

where

$$\beta \left(E_1, E_2, \frac{t_1}{R_0}, \frac{t_2}{R_0} \right) = \frac{6 \left(\frac{t_1}{R_0} + \frac{t_2}{R_0} \right)}{E_1 t_1 \left(\frac{t_1}{R_0} \right)^2 + E_2 t_2 \left(\frac{t_2}{R_0} \right)^2 + 4 \left(\frac{t_1}{R_0} \right)^2 + 4 \left(\frac{t_2}{R_0} \right)^2 + 6 \frac{t_1 t_2}{R_0 R_0}} \quad (2)$$

$$f(\theta_0, r) = \frac{2 \sin(r\theta_0/2) - r\theta_0 \cos(\theta_0/2)}{2 \sin(\theta_0/2)} \quad (3)$$

The ratio of Young's modulus, E_1/E_2 , and the differential CTE, $\Delta\alpha = \alpha_2 - \alpha_1$, are the only factors related to material properties. The effective CTE of the metamaterial α_{meta} is highly sensitive to geometrical parameters t_1/R_0 , t_2/R_0 , θ_0 , r , and the layout of the materials ($\Delta\alpha > 0$ or vice versa).

Figure 1a presents a cross-sectional illustration of the fabrication steps for a representative 2D filamentary microstructure of this type. The bilayer beam consists of a frame layer (polyimide, PI; in yellow) and an actuation layer (poly(methyl methacrylate) (PMMA); in red) bonded to one another along the length of the filament. The process starts with precision laser cutting (ProtoLaser U4) of a film of PI (75 μm thick; AP8535R, DuPont Pyralux; $E_{\text{PI}} \approx 2.5$ GPa, $\alpha_{\text{PI}} \approx 3.0 \times 10^{-5} \text{ K}^{-1}$), into interconnected serpentine filaments. A film of copper (18 μm thick) stiffened by water-soluble tape (OKI-AKW WT-1, Aquasol) serves as a sacrificial support during the cutting. Spin casting and curing at 135 $^\circ\text{C}$ for 10 min yields a uniform coating of PMMA (495 PMMA A5, Microchem; $E_{\text{PMMA}} \approx 2.5$ GPa, $\alpha_{\text{PI}} \approx 7.0 \times 10^{-5} \text{ K}^{-1}$) that fills the open regions between the PI features and coats a thin PMMA layer on its top surface. A second laser cutting process aligned to the first creates matching serpentine features in the PMMA, to complete the fabrication. Removing the tape by rinsing with water and eliminating the copper by wet etching releases the bimaterial network into a freestanding form. Figure 1b shows scanning electron microscope (SEM) images of as-fabricated bilayer

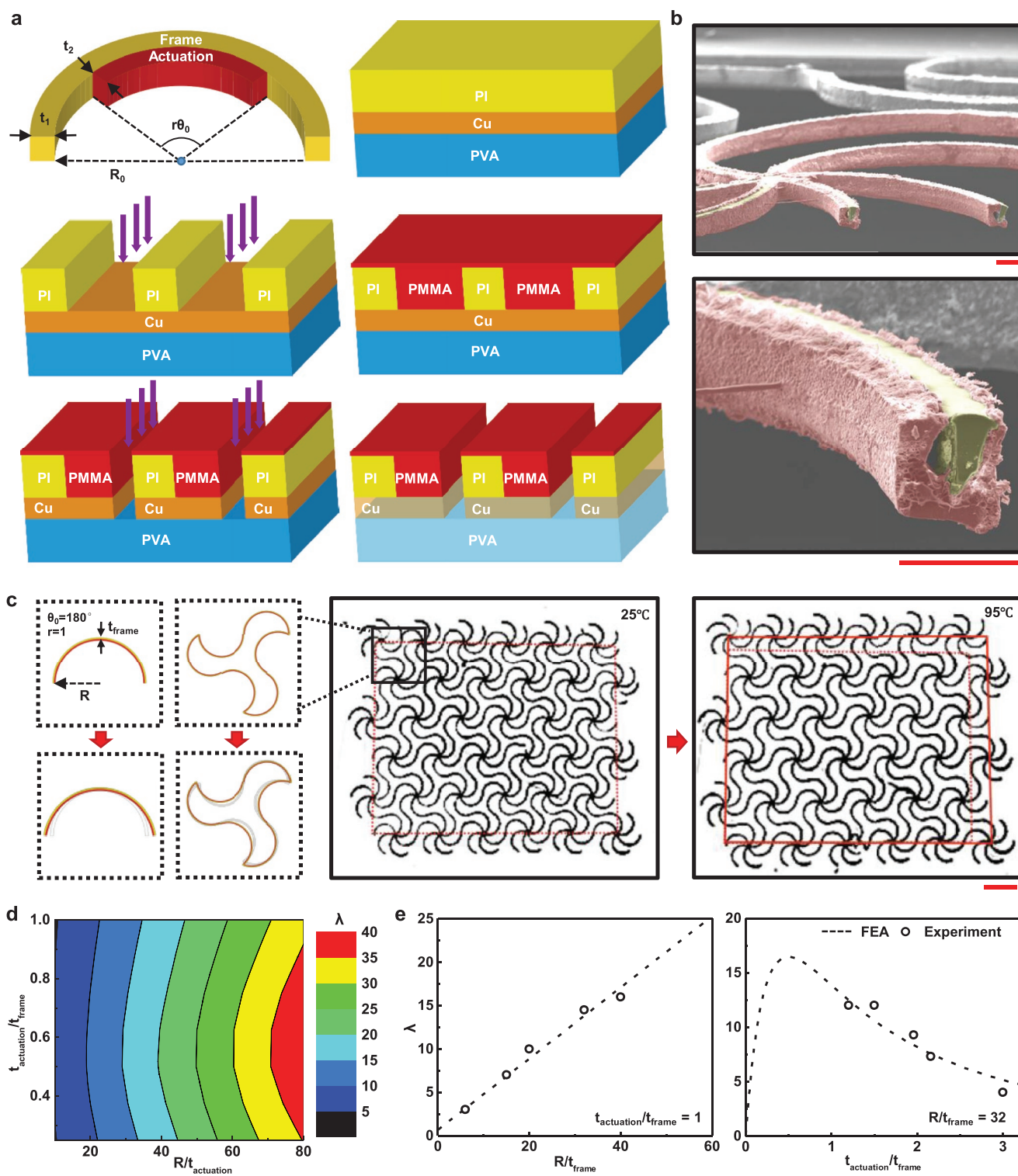


Figure 1. Design, fabrication, and performance of 2D mechanical metamaterials with tunable thermal expansion. a) Cross-sectional schematic illustration of the fabrication process of the interconnected bilayer beams consisting of frame layer (polyimide; in yellow) and actuation layer (polymethylmethacrylate; in red) sandwiched in-plane. b) Scanning electron microscopy (SEM) images of as-fabricated bilayer beams. c) Top view of the computational (left) and experimental (right) results of the 2D serpentine microstructure designed with positive coefficient of thermal expansion (CTE) undergoing heating in an oil bath. d) The computational prediction for the effective CTE versus two tunable geometrical parameters of the serpentine microstructures. e) Experimental measurements of the effective CTE of the metamaterials with independently varied radius to thickness ratio (left) and relative thickness ratio (right), in comparison with the computational prediction. Scale bars, 100 μm (b) and 2 mm (c).

beams. Measurements of the beam thickness from multiple locations across the structure indicate a laser alignment tolerance $\approx 6 \mu\text{m}$. The finished top surface has a maximum height variation of $\approx 10 \mu\text{m}$, where mechanical polishing can help improve the surface quality.

This simple sequence can yield 2D metamaterials with wide ranging types of geometries, limited mainly by the resolution and registration of the laser cutting process. Figure 1c shows a top view of a representative material system in a periodic triangular lattice with all beams designed with the actuation materials (PMMA) on the concave side $\alpha_1 < \alpha_2$, $\theta_0 = \pi$, $r = 1$, $R_0 = 800 \mu\text{m}$, and $t_1 = t_2 = 25 \mu\text{m}$. The particular thickness corresponds to the smallest feature size accessible with our laser cutting system as applied to PI films with thicknesses of $75 \mu\text{m}$. The sample consists of 6×6 unit cells with an overall size of $18 \text{ mm} \times 14 \text{ mm}$. The magnified images on the left show simulations of the behavior of a unit cell due to thermally actuated bending of the curved bilayer beam. Optical images show the resulting expansion due to heating from 25 to $95 \text{ }^\circ\text{C}$ in oil. The effective strain, defined by the edge-to-edge change in dimensions, is $\approx 6.9\%$, which corresponds to a CTE, $\alpha_{\text{meta}} = 1.1 \times 10^{-3} \text{ K}^{-1} \approx 14.0\alpha_{\text{actuation}}$, where $\alpha_{\text{actuation}} = \alpha_{\text{PMMA}}$.

With this frame geometry and constituent materials ($E_{\text{actuation}}/E_{\text{frame}} \approx 1$, $\alpha_{\text{actuation}} - \alpha_{\text{frame}} \approx 0.57\alpha_{\text{actuation}}$), the effective CTE of the metamaterial (Equations (1)–(3)) follows from five nondimensional geometrical parameters: the ratio of the radius to the frame thickness $\gamma = R_0/t_{\text{frame}}$, the ratio of the thickness of the actuation to the frame layers $\xi = t_{\text{actuation}}/t_{\text{frame}}$, the initial angle θ_0 , the covering ratio r , and the convexity $\zeta = \Delta\alpha/|\Delta\alpha|$, as (see Note S1, Supporting Information, for details)

$$\alpha_{\text{meta}}(\gamma, \xi, \zeta, \theta_0, r) \sim \frac{6\xi(1+\xi)}{\xi^4 + 4\xi^3 + 6\xi^2 + 4\xi + 1} \gamma \zeta f(\theta_0, r) \alpha_{\text{actuation}} \quad (4)$$

Figure 1d shows the results of finite element analysis (FEA; see the Experimental Section for details) for the scaled CTE $\lambda = \alpha_{\text{meta}}/\alpha_{\text{actuation}}$ versus R_0/t_{frame} and $t_{\text{actuation}}/t_{\text{frame}}$, with a fixed initial angle, $\theta_0 = \pi$. The measurements in Figure 1e are consistent with the FEA results for the dependence on R_0/t_{frame} (left) and $t_{\text{actuation}}/t_{\text{frame}}$ (right), where $R_0/t_{\text{frame}} = 32$, $t_{\text{actuation}}/t_{\text{frame}} = 1$, $\theta_0 = \pi$, $\zeta r = 1$, and $t_{\text{frame}} = 25 \mu\text{m}$. With this default geometry (used throughout the manuscript unless otherwise stated), the computed CTE is $\lambda = 13.8$. The observation that the effective CTE increases monotonically with R_0/t_{frame} but has a global maximum at $t_{\text{actuation}}/t_{\text{frame}} = 0.5$ agrees with the analytical prediction (Note S1 and Figure S2a,b, Supporting Information). The normalized modulus $E_{\text{meta}}/E_{\text{frame}} = (5.1 \pm 1.8) \times 10^{-5}$ is within an order of magnitude of the theoretical predictions (Note S2 and Figure S4, Supporting Information). FEA indicates that system size does not affect the CTE of the metamaterials (Figure S5, Supporting Information).

In addition to simple positive, isotropic thermal expansion behaviors, unusual possibilities follow from other choices of the geometrical parameters of the triangular unit cells. Figure 2 presents three representative designs for metamaterials that exhibit negative, anisotropic, and shear modes of thermal expansion. The top row shows optical images of the unit cell,

the middle row shows images of the response to a default heating condition (oil bath, $\Delta T = 80 \text{ }^\circ\text{C}$), and the bottom row presents comparisons of FEA to experimental results. The designs focus on the initial covering angle of the three beams, $\theta_i = \zeta r \theta_0$ ($i = 1, 2, 3$) (Note S1 and Figure S2c, Supporting Information). Switching the actuation materials to the convex side ($\zeta = -1$) yields negative CTE of the unit beam. Figure 2a shows a unit cell in which all beams have negative convexity, $\theta_1 = \theta_2 = \theta_3 = -\pi$. The regions highlighted in red and yellow correspond to actuation and frame materials, separately. After heating, the metamaterial shrinks by $\approx 6.8\%$. The corresponding CTE, $\alpha_{\text{meta}} = -8.5 \times 10^{-4} \text{ K}^{-1} \approx -12.2\alpha_{\text{actuation}}$, agrees with the FEA results. The FEA also predicts that the negative CTE scales proportionally with R_0/t_{frame} , consistent with the behavior of its positive counterpart.

Tuning the geometrical parameters of each beam of the unit cell can yield anisotropic thermal deformations. When the arc angle of the frame layer θ_0 is fixed at π , the magnitude of the thermal deformation of a beam can be tuned through control of the covering ratio r (Note S1 and Figure S2c, Supporting Information). Figure 2b shows a design with the beam along x -axis of angle $\theta_1 = -\pi/2$ and the other beams of angle $\theta_2 = \theta_3 = +\pi$. The resulting structure exhibits a thermal expansion of $\approx 7.8\%$ along the y -axis but $\approx 0\%$ along the x -axis for a ΔT of $80 \text{ }^\circ\text{C}$. The CTE along the y -direction, $\lambda_y \approx 13.4$ is comparable to that of the isotropic case. The FEA results show that as θ_1 approaches $-\pi/2$ from the positive side, the x -axis CTE λ_x decreases to zero while λ_y remains at ≈ 15.0 . Figure 2c shows that the combination of $\theta_1 = -\pi/2$, $\theta_2 = +\pi$, and $\theta_3 = -\pi$ generates an unusual shear mode of thermal expansion. With a ΔT of $80 \text{ }^\circ\text{C}$, the sample shears by $\approx 4.7^\circ$. The magnitude of the CTE associated with this shear mode, defined in terms of the shear strain, depends on the radius to thickness ratio. FEA results predict that the shear CTE of this type of metamaterial increases linearly with R/t_{frame} , similar to the case of its isotropic counterparts.

The fabrication methodology also allows for geometries that vary spatially across unit cells in a given system. Figure 3a shows an example design comprising cells with both positive (indicated in red) and negative (blue) CTE in four adjacent areas. The anisotropic expansion and contraction behaviors produce an overall shear and rotation. Figure 3b presents another design consisting of two strips of cells with positive and negative CTE. The tension and compression associated with the positive and negative regions, respectively, induce a bending moment of the overall construct. A design of cells with monotonically increasing CTE along one spatial axis leads to a gradient mode of thermal expansion along that axis. For example, as shown in Figure 3c, a system that includes unit cells in which $\xi = t_{\text{actuation}}/t_{\text{frame}}$ gradually decreases from 3:1 to 1:1 yields a corresponding spatial gradient in CTE. For the case where the CTE changes for every other column, a network with an overall rectangular shape expands upon heating into one with a trapezoid shape with a taper angle of $\theta_{\text{taper}} \approx 1^\circ$. Figure 3d shows corresponding FEA results, where the insets indicate the deformation mode. Experiments indicate that the shear angle $\theta_{\text{shear}} \approx 7^\circ$ and bending angle $\theta_{\text{bending}} \approx 20^\circ$ for a ΔT of $80 \text{ }^\circ\text{C}$, in agreement with FEA. FEA also yields predictions for the dependence of the shear angle

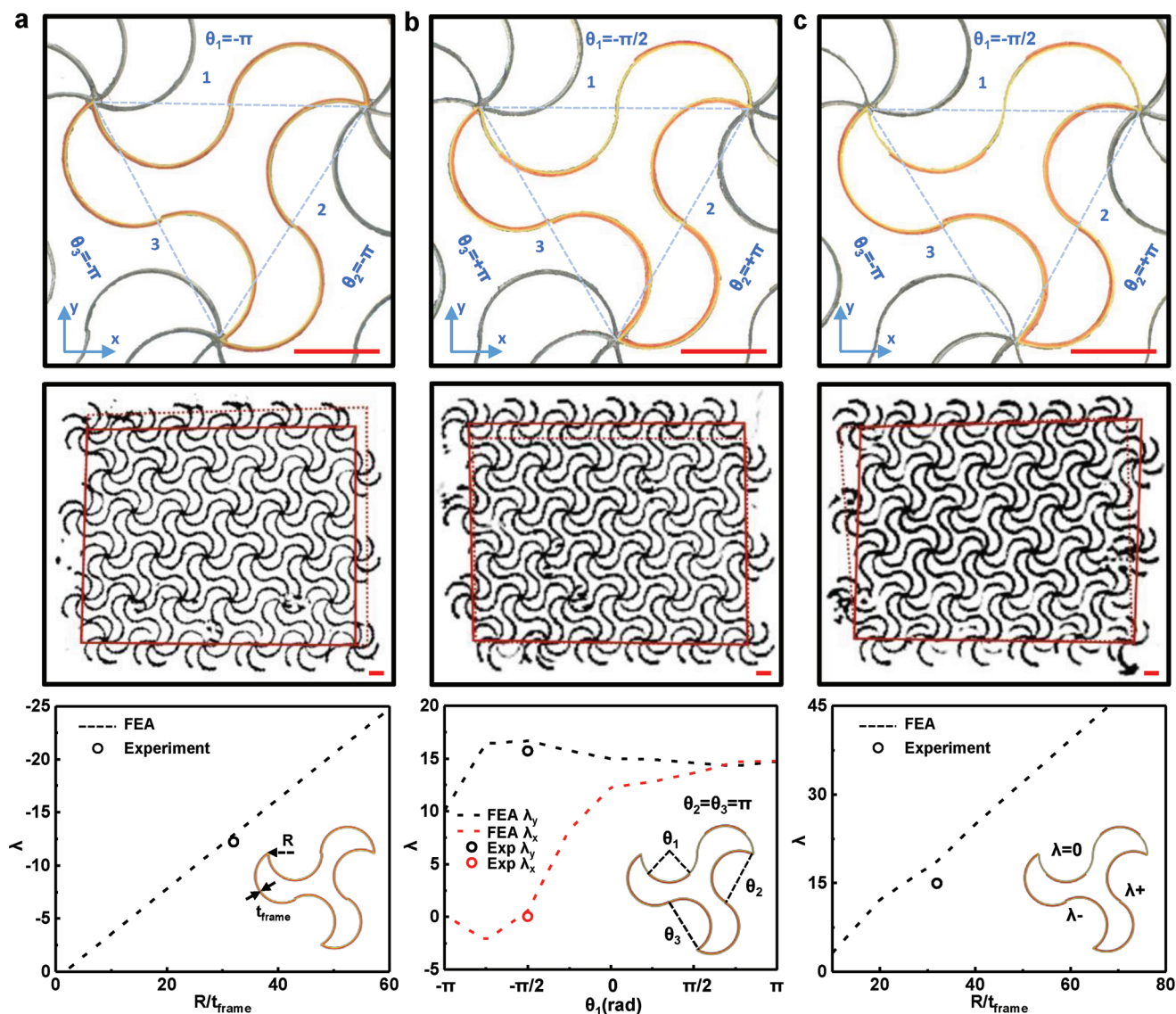


Figure 2. Precise control of bimaterial layout for unusual thermal expansion. a–c) Optical images and FEA results of metamaterials designed for negative, anisotropic, and shear deformation under thermal expansion. Top: One unit cell of the designed microstructure. Middle: The material under heating ($\Delta T = 80\text{ }^\circ\text{C}$) in an oil bath. The dashed/solid lines track the undeformed/deformed states of the materials. Bottom: Computational prediction for the anisotropic design of effective CTE with the inset illustrating the design principle based on the covering angle of the actuation layer. Scale bars, 1 mm.

on R/t_{frame} and the bending angle on aspect ratio (width vs length), with other parameters fixed (Figure 3d).

As illustrated in Figure 4a, a spatially uniform frame layer bonded to the base of the serpentine structures leads to out-of-plane (z -axis) bending upon thermal actuation. The 3D bending of a homogenous and isotropic precursor structure is stable and deterministic (Figure S6, Supporting Information). Figure 4b highlights the simple scheme for realizing this type of structure. Here, the laser cutting process removes only a well-defined fraction of the full thickness of the PI film. The second cutting step then removes both the PMMA and the residual PI into the selected serpentine contours.

A key parameter that determines the magnitude of the z -axis bending of the metamaterials is the ratio of the thickness of

the top actuation and bottom frame layers h_1/h_2 . Figure 4c shows a side view of a metamaterial designed using the default 2D parameters and $h_1/h_2 = 1.0$, for the case of a $100\text{ }^\circ\text{C}$ temperature change induced by placing the sample in an oven. The top row shows the thermal bending response. At room temperature, the structure, with a bottom PI thickness of $37.5\text{ }\mu\text{m}$ curves upward due to residual stresses in the films associated with PMMA curing. Viewed from the wider side (18 mm) of a structure with 6×6 unit cells, the bending angle θ_T is initially 52° . Upon heating from $30\text{ }^\circ\text{C}$, the film bends toward the bottom frame material and eventually reaches a planar state at $130\text{ }^\circ\text{C}$. In the bottom row, the FEA simulates a process heating a metamaterial with zero initial bending from 30 to $130\text{ }^\circ\text{C}$. Because the observed bending is linear and reversible,

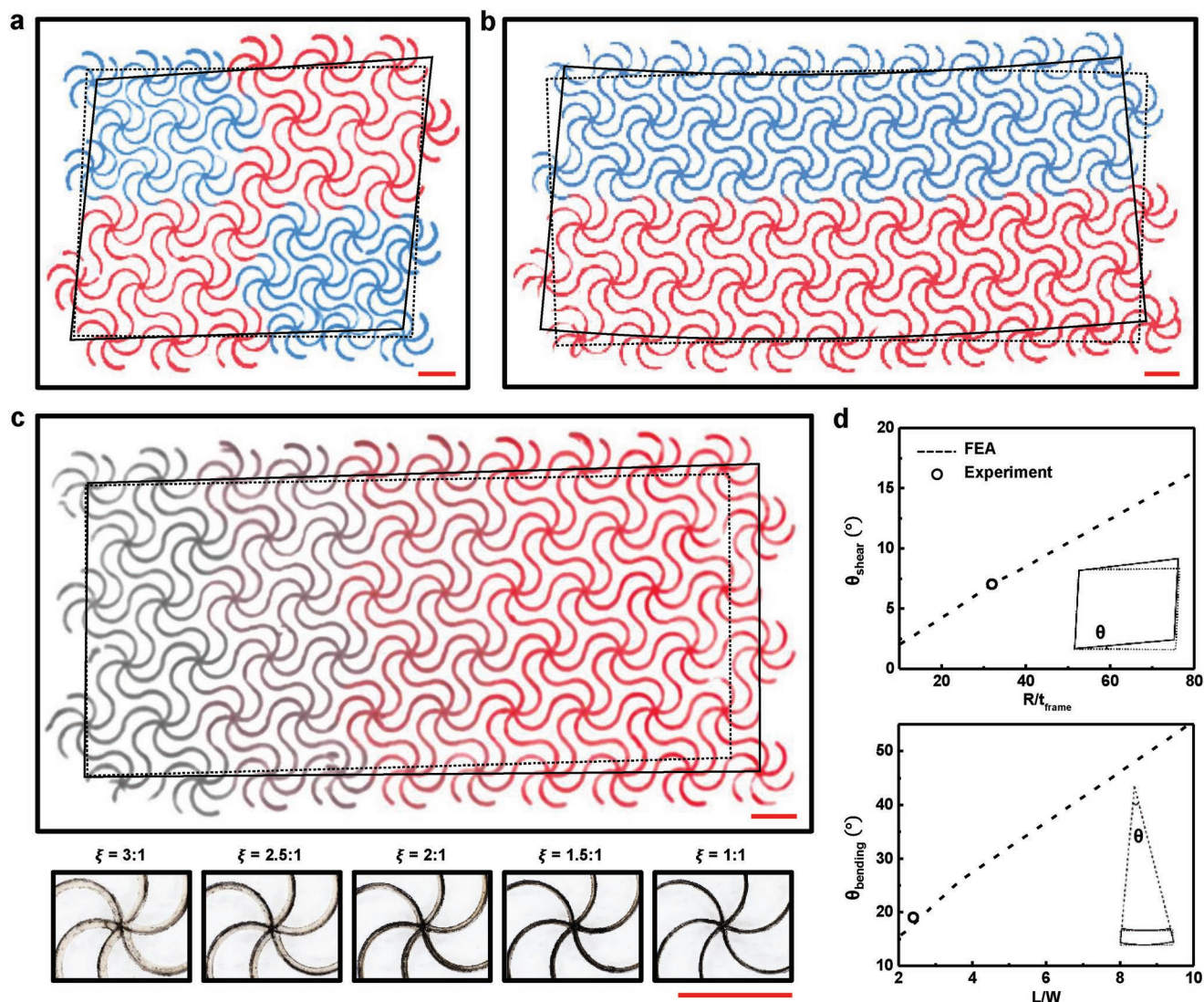


Figure 3. Hierarchical manipulation of microstructures for unusual thermal expansion. a–c) Optical images of metamaterials designed for shear, bending, and gradient deformation under thermal expansion, based upon spatial arrangement of unit cells with different CTE. Red and blue differentiate cells with positive/negative CTE. The dashed and solid lines track the deformation of materials under room temperature and under heating ($\Delta T = 80^\circ\text{C}$). The bottom row of (c) shows zoomed-in optical images of representative cells in every other two columns of the material. d) Computational prediction for the shear angle versus radius-to-thickness ratio with the inset indicating the deformation mode. Top: The experimental measurement from (a) agrees with the prediction. Bottom: Computational prediction for the bending angle versus the aspect ratio in the bending direction with the inset indicating the deformation mode. The experimental result from (b) is close to the prediction. Scale bars, 2 mm.

an initial residual stress is equivalent to an elastic thermal stress. The mechanical response of the reverse actuation is analogous to a cooling process. Figure 4d provides a quantitative comparison between experiment and FEA, where the change of bending angle $\Delta\theta_T$ due to heating agrees within 6° . Figure 4e shows FEA results for the dependence of bending on h_1/h_2 and on R/t_{frame} .

Dynamically tunable actuation of metamaterial structures can be achieved by Joule heating with integrated conductive elements. The simplest scheme uses a thin bilayer of Ti ($\approx 10\text{ nm}$)/Au ($\approx 120\text{ nm}$) deposited uniformly onto the top surfaces of the structures. Increases in temperature of $>100^\circ\text{C}$ can be achieved with $\approx 1\text{ mW mm}^{-2}$ power.^[34] Under a spatially uniform heating condition, it is reasonable to assume that convective heat

transfer dominates the dissipation mechanism. The governing rate equation for the thermal response at room temperature T_a becomes

$$cm \frac{dT}{dt} = Q - \eta A(T - T_a) \quad (5)$$

where c is the specific heat capacity, m is the mass of the material, Q is the energy influx, A is the surface area, and η is the heat transfer coefficient of air assumed to take a constant value of $30 \times 10^{-6}\text{ W mm}^{-2}\text{ K}^{-1}$. The solution to Equation (5) is

$$T = (T_0 - T_a)(1 - e^{-t/\tau}) + T_a \quad (6)$$

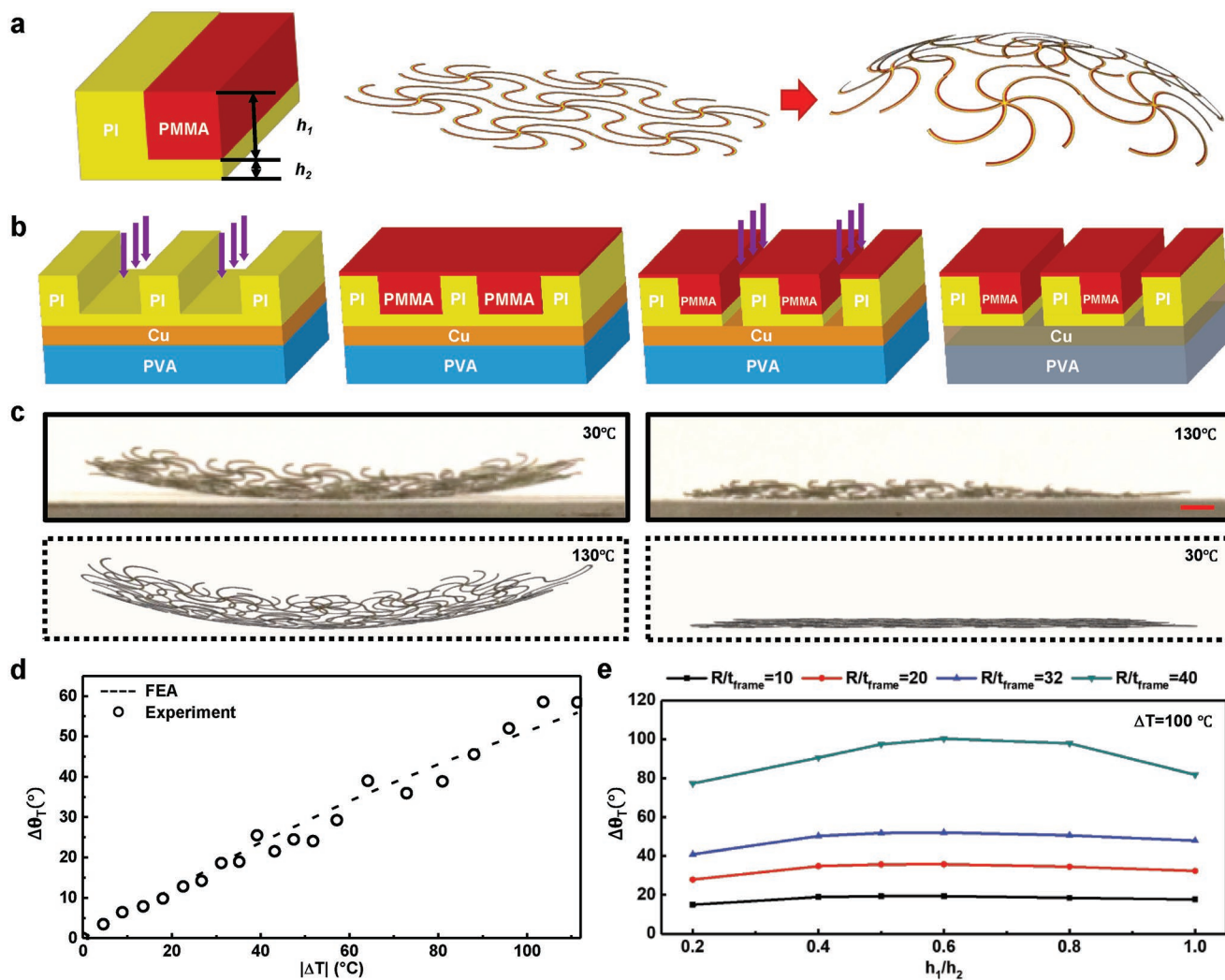


Figure 4. Tunable thermal expansion in three dimensions. a) Cross-sectional schematic illustration of the design concept, predicted deformation mode, and b) fabrication process of the interconnected bilayer beams sandwiched in-plane and out-of-plane for 3D thermal expansion. c) Side view of the computational (bottom) and experimental (top) results of the 3D metamaterials ($h_1/h_2 = 1$, $R/t_{\text{frame}} = 32$) undergoing heating in oven. The as-fabricated material is precurved due to residual stress. d) Computational prediction for the out-of-plane bending angle over temperature change. e) Experimental measurements of the bending angle versus tunable geometrical parameters of the 3D microstructures. Scale bars, 2 mm.

where $T_0 = Q/\eta A + T_a$ is the steady-state temperature at thermal equilibrium. The relaxation time constant is $\tau = cm/\eta A$. The filamentary designs yield a low thermal mass and large surface area for fast thermal relaxation and, therefore, fast switching times. The thin metal coatings do not perturb the mechanics significantly.

Figure 5a shows a structure in a layout for isotropic, positive CTE (default dimensions and thicknesses), coated with the Ti/Au thermal actuator. Figure 5b shows on the right the analytical prediction of the thermal response of a 10×10 unit-cell metamaterial ($18 \text{ mm} \times 14 \text{ mm}$). This structure has a surface area that is ≈ 5 times larger than that of a uniform thin film with the same thickness and overall area. Given materials properties with specific heat capacity $c_{\text{PI}} = 1090 \text{ J kg}^{-1} \text{ K}^{-1}$, $c_{\text{PMMA}} = 1466 \text{ J kg}^{-1} \text{ K}^{-1}$, and mass density $\rho_{\text{PI}} = 1.42 \times 10^{-6} \text{ kg mm}^{-3}$, $\rho_{\text{PMMA}} = 1.18 \times 10^{-6} \text{ kg mm}^{-3}$, the predicted relaxation time constant for the material is $\tau = 0.8 \text{ s}$.

For an ambient temperature of $28 \text{ }^\circ\text{C}$, applying 1 W of electrical power leads to an approximately uniform steady-state temperature of $115 \text{ }^\circ\text{C}$, as shown in the infrared (IR) images in the left part of Figure 5b. Fitting the time response data with an exponential function (Equation (4)) for eight cycles of on/off events yields a time constant of $\tau = 0.45 \pm 0.04 \text{ s}$.

Changing the heating method and/or location provides additional flexibility. Connecting a current source to patterned thermal actuator electrodes yields different heating paths. Figure 5c presents a scheme where eight conducting pads surround the sample. The top IR images correspond to different heating modes. The bottom figures give corresponding contour maps of von Mises strain and displacement vectors for each of the unit cells, reconstructed from optical images (Notes S3 and S4; Figures S7 and S8, Supporting Information). The overlay is an image of the thermally deformed material. The elastic coupling between unit cells together with the

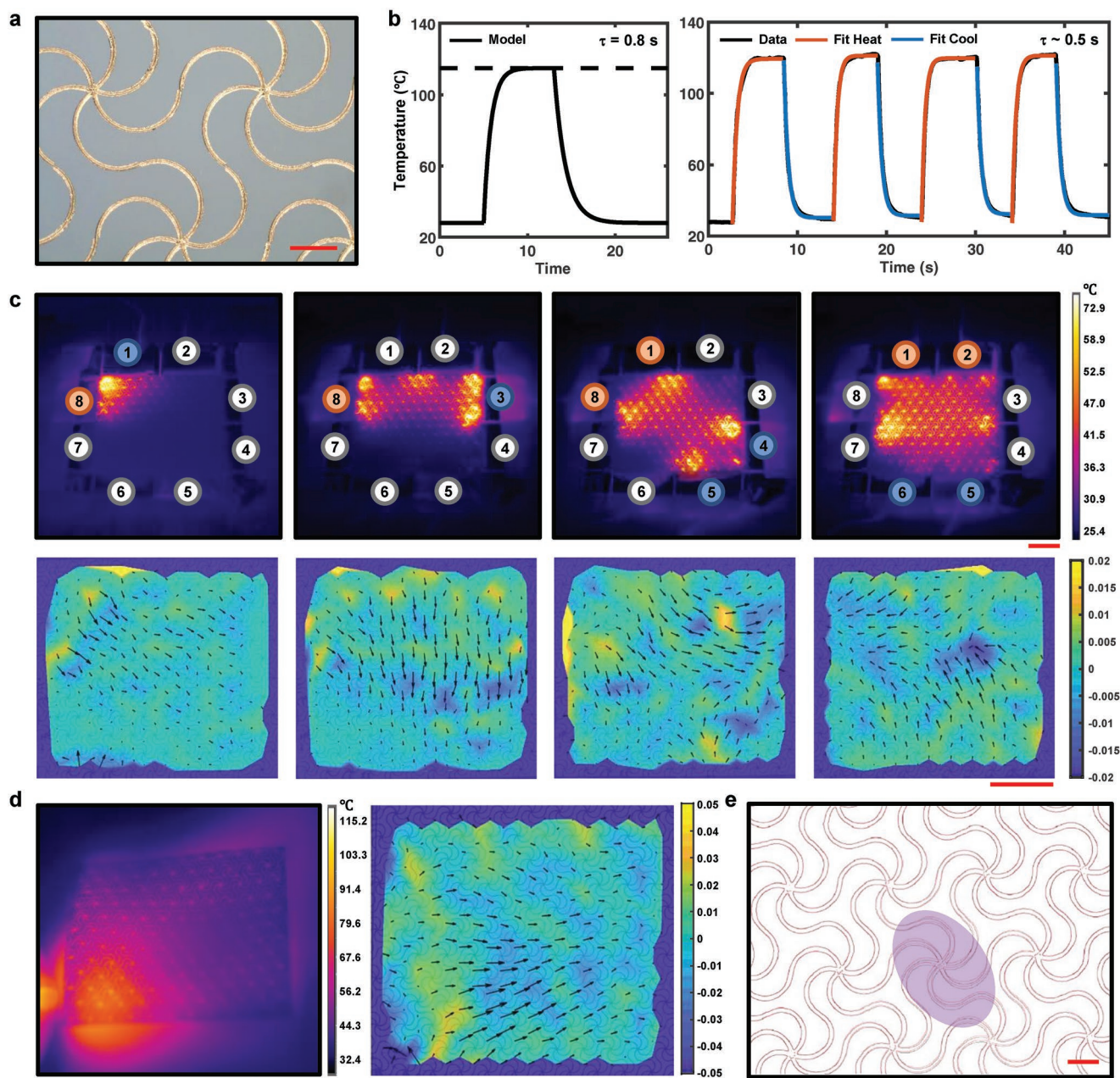


Figure 5. Implementation of diverse local heating modes. a) Optical image of a unit cell deposited with 10 nm Ti and 120 nm Au for electrothermal actuation through joule heating. b) Simulation (left) and experimental (right) results showing ≈ 1 s thermal response time to the electrical actuation. c) Top: Infrared (IR) thermographs collected during joule heating with an input power of ≈ 1 W supplied via different nodes marked in red and blue. Bottom: the corresponding strain contour and displacement vector map of the triangular units, constructed from the optical image recordings of deforming lattice. Overlaid is the image of material under heating. d) Left: IR thermographs collected when the left corner of a sample is heated by a stream of hot air. Right: the corresponding strain contour and displacement vector map of the triangular units, overlaid with the image of material under heating. e) Edge contours of a sample material before (black) and under (red) a confined ultraviolet (UV) exposure (shaded in purple) showing a rotation of a unit cell induced by local optical heating. Scale bars, 1 mm (a,e) and 1 cm (c,d).

rigid-frame boundary conditions produce complex strain profiles in these different cases.

Applying directed hot/cold air flow to the sample can further localize the thermal expansion. Figure 5d shows on the left an IR image collected as a heat gun delivers a stream of hot air (AOYUE Int866) to the lower left corner of a sample. The right figure is the corresponding strain and displacement vector

maps, overlaid with an image of the material during heating. Light absorption provides yet another option. Figure 5e shows the thermal response of a sample during illumination with an ultraviolet (UV) beam with a laser power of ≈ 300 mW. The unit cell under illumination with an intensity of 1.7 mW mm^{-2} undergoes local heating and a corresponding displacement by a maximum of $\approx 20 \text{ }\mu\text{m}$ ($0.8t_{\text{frame}}$). The various available local

heating methods create opportunities for shape morphing of metastructures with various designs and CTE behaviors (Figure S9, Supporting Information).

In conclusion, the results presented here establish the experimental and computational basis for a 2D mechanical metamaterial platform that can support widely tunable thermal deformations, including the ability to achieve an arbitrary CTE tensor. Here, controlling the radius and thickness of the filamentary beams in these constructs provides tunability over the magnitude of thermal deformation. Changing the covering angle of each beam in a system with triangular unit cells introduces highly anisotropic tuning of the thermal expansion behavior, which decouples the principal-axis terms and provides access to off-diagonal terms in the CTE tensor. In addition to the beam-level design aspects, the strong interactions between cells allow for a cell-level blending of lattices with different CTE for additional unusual modes of thermal expansion. Examples of shearing, bending, and gradient modes reported here are simple illustrations of concepts that can support complex morphing structures. Incorporating electrical or optical sources of thermal power into these systems yields fast, controlled modes of switching through local heating. Compared to other functionally similar mechanical metamaterials or actuation schemes that rely on ionic concentrations, hydration, pH gradients, or light exposures,^[35–38] the platforms presented here offer advantages and unique aspects in wide-range tunability, few limitations in materials selection, fast response time, deterministic local control of responses, and easy integration with other electronic components. As such, these concepts have the potential to serve as a versatile, active, and dynamic pathway to topology optimization^[39–43] or coordinate transformations^[44–47] in mechanical metamaterials.

Experimental Section

Fabrication of the Metamaterials: The fabrication process started with a metallized sheet of PI (75 μm thick PI with 18 μm copper on both sides, AP8535R, DuPont Pyralux). After removing the copper layer on one side using wet etching (CE-100 copper etchant, Transense, 15 min), four pieces of water-soluble tapes (OKI-AKW WT-1, Aquasol) applied to the other side stiffened the copper substrate. Laser cutting (ProtoLaser U4, LPKF) removed PI in selected regions with controlled removal depth. Drop-casting coated a layer ($\approx 0.08 \pm 0.01 \text{ mL cm}^{-2} \approx 75 \mu\text{m}$ thickness) of PMMA (495 PMMA A5, Microchem) on the patterned PI layer. Laser cutting removed selected regions of the sample. Rinsing the sample with deionized (DI) water to remove the water-soluble tape and wet etching to remove the copper layer. Graphite aerosol (Aerodag G, Ted Pella) spray-coated the sample for IR imaging.

Finite Element Analyses: FEA was carried out on the commercial software ABAQUS. Four-node shell elements (S4R) were used for the PI and PMMA; refined meshes were adopted to ensure computational accuracy. PI and PMMA were all simplified as linear elastic materials whose elastic modulus (E) and Poisson's ratio (ν) are $E_{\text{PI}} = 2.5 \text{ GPa}$, $\nu_{\text{PI}} = 0.34$ for PI, and $E_{\text{PMMA}} = 2.5 \text{ GPa}$, $\nu_{\text{PMMA}} = 0.3$ for PMMA. And the linear thermal expansion coefficients (α) of PI and PMMA are $\alpha_{\text{PI}} \approx 3.0 \times 10^{-5} \text{ K}^{-1}$ and $\alpha_{\text{PMMA}} = 7.0 \times 10^{-5} \text{ K}^{-1}$, respectively.

Characterization of the Mechanical Properties: Tensile testing (Mark-10 ESM303) of five samples yielded the stress–strain relationships across a range of strains from 0 to 10%. A first-order polynomial fit to the data yielded the Young's modulus. The strain rate was 10^{-3} s^{-1} .

Data Analytics: Lattice nodes digitization used Web plot digitizer (<https://github.com/ankitrohatgi/WebPlotDigitizer.git>). Thermal expansion measurement used ImageJ 1.x (<https://github.com/imagej/imagej1.git>). All analysis used MATLAB (R2018b) technical computing languages.

Supporting Information

Supporting Information is available from the Wiley Online Library or from the author.

Acknowledgements

X.N. and X.G. contributed equally to this work. X.N. and J.A.R. acknowledge support from a ARO MURI program. Y.Z. acknowledges support from the National Natural Science Foundation of China (Nos. 11672152 and 11722217), the Tsinghua National Laboratory for Information Science and Technology and the State Key Laboratory of Digital Manufacturing Equipment and Technology, Huazhong University of Science and Technology (No. DMETF2019005). X.G. acknowledges support from National Natural Science Foundation of China (No. 11702155). Y.H. acknowledges support from the NSF (Grant No. CMMI1635443).

Conflict of Interest

The authors declare no conflict of interest.

Keywords

bimaterial lattices, programmable metamaterials, strain-field engineering, tunable thermal properties, unusual thermal expansion

Received: August 20, 2019

Revised: September 18, 2019

Published online: October 9, 2019

- [1] M. R. Werner, W. R. Fahrner, *IEEE Trans Ind. Electron.* **2001**, *48*, 249.
- [2] J. Varghese, T. Joseph, M. T. Sebastian, *Mater. Lett.* **2011**, *65*, 1092.
- [3] C. Lind, *Materials* **2012**, *5*, 1125.
- [4] H. Tu, H. Jiang, H. Yu, Y. Xu, *Appl. Phys. Lett.* **2013**, *103*, 241902.
- [5] G. Stoychev, N. Pureskiy, L. Ionov, *Soft Matter* **2011**, *7*, 3277.
- [6] C. Yu, Y. Pan, H. Ma, T. Ma, J. Zhang, Y. Song, M. Y. S. Kalani, L. Dai, H. Jiang, *Macromol. Rapid Commun.* **2011**, *32*, 820.
- [7] J. C. Breger, C. Yoon, R. Xiao, H. R. Kwag, M. O. Wang, J. P. Fisher, T. D. Nguyen, D. H. Gracias, *ACS Appl. Mater. Interfaces* **2015**, *7*, 3398.
- [8] W. Xu, Z. Qin, C. T. Chen, H. R. Kwag, Q. Ma, A. Sarkar, M. J. Buehler, D. H. Gracias, *Sci. Adv.* **2017**, *3*, e1701084.
- [9] J. Guo, T. Shroff, C. K. Yoon, J. Liu, J. C. Breger, D. H. Gracias, T. D. Nguyen, *Extreme Mech. Lett.* **2017**, *16*, 6.
- [10] Z. Ding, C. Yuan, X. Peng, T. Wang, H. J. Qi, M. L. Dunn, *Sci. Adv.* **2017**, *3*, e1602890.
- [11] K. H. Matlack, M. Serra-Garcia, A. Palermo, S. D. Huber, C. Daraio, *Nat. Mater.* **2018**, *17*, 323.
- [12] A. L. Goodwin, M. Calleja, M. J. Conterio, M. T. Dove, J. S. O. Evans, D. A. Keen, L. Peters, M. G. Tucker, *Science* **2008**, *319*, 794.
- [13] S. Iikubo, K. Kodama, K. Takenaka, H. Takagi, M. Takigawa, S. Shamoto, *Phys. Rev. Lett.* **2008**, *101*, 205901.

- [14] C. W. Li, X. Tang, J. A. Muñoz, J. B. Keith, S. J. Tracy, D. L. Abernathy, B. Fultz, *Phys. Rev. Lett.* **2011**, *107*, 195504.
- [15] D. Das, T. Jacobs, L. J. Barbour, *Nat. Mater.* **2010**, *9*, 36.
- [16] A. D. Fortes, E. Suard, K. S. Knight, *Science* **2011**, *331*, 742.
- [17] R. Lakes, *J. Chem. Inf. Model.* **1996**, *53*, 1689.
- [18] O. Sigmund, S. Torquato, *Appl. Phys. Lett.* **1996**, *69*, 3203.
- [19] R. Lakes, *Appl. Phys. Lett.* **2007**, *90*, 221905.
- [20] C. S. Ha, E. Hestekin, J. Li, M. E. Plesha, R. S. Lakes, *Phys. Status Solidi B* **2015**, *252*, 1431.
- [21] J. Qi, J. W. Halloran, *J. Mater. Sci.* **2004**, *39*, 4113.
- [22] A. Takezawa, M. Kobashi, M. Kitamura, *APL Mater.* **2015**, *3*, 076103.
- [23] Q. Wang, J. A. Jackson, Q. Ge, J. B. Hopkins, C. M. Spadaccini, N. X. Fang, *Phys. Rev. Lett.* **2016**, *117*, 175901.
- [24] C. A. Steeves, S. L. dos Santos e Lucato, M. He, E. Antinucci, J. W. Hutchinson, A. G. Evans, *J. Mech. Phys. Solids* **2007**, *55*, 1803.
- [25] N. M. A. Palumbo, C. W. Smith, W. Miller, K. E. Evans, *Acta Mater.* **2011**, *59*, 2392.
- [26] E. Gdoutos, A. A. Shapiro, C. Daraio, *Exp. Mech.* **2013**, *53*, 1735.
- [27] N. Yamamoto, E. Gdoutos, R. Toda, V. White, H. Manohara, C. Daraio, *Adv. Mater.* **2014**, *26*, 3076.
- [28] W. Miller, D. S. Mackenzie, C. W. Smith, K. E. Evans, *Mech. Mater.* **2008**, *40*, 351.
- [29] L. Wu, B. Li, J. Zhou, *ACS Appl. Mater. Interfaces* **2016**, *8*, 17721.
- [30] K. Wei, H. Chen, Y. Pei, D. Fang, *J. Mech. Phys. Solids* **2016**, *86*, 173.
- [31] H. Xu, A. Farag, D. Pasini, *J. Mech. Phys. Solids* **2018**, *117*, 54.
- [32] H. Zhu, T. Fan, Q. Peng, D. Zhang, *Adv. Mater.* **2018**, *30*, 1705048.
- [33] E. Boatti, N. Vasios, K. Bertoldi, *Adv. Mater.* **2017**, *29*, 1700360.
- [34] C. Cardenas, D. Fabris, S. Tokairin, F. Madriz, C. Y. Yang, *J. Heat Transfer* **2012**, *134*, 111401.
- [35] C. Keplinger, J. Y. Sun, C. C. Foo, P. Rothmund, G. M. Whitesides, Z. Suo, *Science* **2013**, *341*, 984.
- [36] H. Zhang, X. Guo, J. Wu, D. Fang, Y. Zhang, *Sci. Adv.* **2018**, *4*, eaar8535.
- [37] X. Chen, W. Li, W. Zhong, Y. Lu, T. Yu, *J. Appl. Polym. Sci.* **1997**, *65*, 2257.
- [38] Q. Zhang, J. Wommer, C. O'Rourke, J. Teitelman, Y. Tang, J. Robison, G. Lin, J. Yin, *Extreme Mech. Lett.* **2017**, *11*, 111.
- [39] P. M. Reis, H. M. Jaeger, M. van Hecke, *Extreme Mech. Lett.* **2015**, *5*, 25.
- [40] A. Clausen, F. Wang, J. S. Jensen, O. Sigmund, J. A. Lewis, *Adv. Mater.* **2015**, *27*, 5523.
- [41] S. V. Kalinin, B. G. Sumpter, R. K. Archibald, *Nat. Mater.* **2015**, *14*, 973.
- [42] C. Schumacher, B. Bickel, J. Rys, S. Marschner, C. Daraio, M. Gross, *ACM Trans. Graphics* **2015**, *34*, 136:1.
- [43] C. Coulais, E. Teomy, K. De Reus, Y. Shokef, M. Van Hecke, *Nature* **2016**, *535*, 529.
- [44] D. Schurig, J. J. Mock, B. J. Justice, S. A. Cummer, J. B. Pendry, A. F. Starr, D. R. Smith, *Science* **2006**, *314*, 977.
- [45] A. Silva, F. Monticone, G. Castaldi, V. Galdi, A. Alù, N. Engheta, *Science* **2014**, *343*, 160.
- [46] T. Bückmann, M. Thiel, M. Kadic, R. Schittny, M. Wegener, *Nat. Commun.* **2014**, *5*, 4130.
- [47] T. Frenzel, M. Kadic, M. Wegener, *Science* **2017**, *358*, 1072.